Monthly Notices
of the
ROYAL ASTRONOMICAL SOCIETY

MNRAS **509,** L11–L16 (2022)
Advance Access publication 2021 October 8

https://doi.org/10.1093/mnrasl/slab113

Measuring the smearing of the Galactic 511-keV signal: positron propagation or supernova kicks?

Thomas Siegert [1]★ Roland M. Crocker [2] Oscar Macias [3,4] Fiona H. Panther [5,6] Francesca Calore,[7] Deheng Song [8] and Shunsaku Horiuchi[3,8]

[1]*Institut für Theoretische Physik und Astrophysik, Universität Würzburg, Campus Hubland Nord, Emil-Fischer-Straße 31, D-97074 Würzburg, Germany*
[2]*Research School of Astronomy and Astrophysics, Australian National University, Canberra, ACT 2611, Australia*
[3]*Kavli IPMU (WPI), UTIAS, The University of Tokyo, Kashiwa, Chiba 277-8583, Japan*
[4]*GRAPPA Institute, University of Amsterdam, NL-1098 XH Amsterdam, The Netherlands*
[5]*Department of Physics, University of Western Australia, Crawley, WA 6009, Australia*
[6]*Australian Research Council Centre of Excellence for Gravitational Wave Discovery (OzGrav), Hawthorn, VIC 3122, Australia*
[7]*CNRS, LAPTh, Université Grenoble-Alpes, Université Savoie Mont Blanc, F-74940 Annecy, France*
[8]*Center for Neutrino Physics, Department of Physics, Virginia Tech, Blacksburg, VA 24061, USA*

Accepted 2021 September 30. Received 2021 September 30; in original form 2021 September 9

ABSTRACT

We use 15 yr of γ-ray data from *INTEGRAL*/SPI in a refined investigation of the morphology of the Galactic bulge positron annihilation signal. Our spatial analysis confirms that the signal traces the old stellar population, revealing for the first time that it traces the boxy bulge and nuclear stellar bulge, while disfavouring the presence of additional dark matter components. Using a three dimensional (3D) smoothing kernel, we find that the signal is smeared out over a characteristic length scale of 150 ± 50 pc, suggesting either annihilation *in situ* at astrophysical sources kicked at formation or positron propagation away from sources. The former is disfavoured due to its requirement of kick velocities different between the Galactic nucleus ($\gtrsim 50\,\mathrm{km\,s^{-1}}$) and wider bulge ($\lesssim 15\,\mathrm{km\,s^{-1}}$) source. Positron propagation prior to annihilation can explain the overall phenomenology of the 511 keV signal for positrons injection energies $\lesssim$1.4 MeV, suggesting a nucleosynthesis origin.

Key words: cosmic rays – Galaxy: bulge – dark matter – gamma-rays: ISM – gamma-rays: stars.

1 INTRODUCTION

The strongest persistent, diffuse γ-ray line signal is found at 511 keV photon energies and originates from the annihilation of positrons with electrons. This signal was first detected by a balloon-borne instrument in 1969 (Johnson & Haymes 1973). The line's flux, of the order of 10^{-3} photons $\mathrm{cm^{-2}\,s^{-1}}$, indicates an annihilation rate of $10^{50}\,\mathrm{e^{+}\,yr^{-1}}$, with a high concentration in the Galactic bulge (Purcell et al. 1997), but the origins of the vast amount of antimatter implied are still unclear (Prantzos et al. 2011). Theoretical expectations associate astrophysical positron sources with regions hosting ongoing star formation in the Galactic disc, leading to an expected bulge-to-disc luminosity ratio of $(B/D)_{511} \lesssim 0.5$. This expectation has been enduringly confounded by measurements, the most recent of which point to $(B/D)_{511} \sim 1$ (Siegert et al. 2016b). This anomaly has been interpreted in two ways: Either positrons propagate away from their putative disc sources, becoming subsequently trapped in the Galactic bulge (e.g. Prantzos 2006; Higdon, Lingenfelter & Rothschild 2009), or a central source populates the bulge by positron transport, either diffusive (Jean et al. 2009; Martin et al. 2012; Alexis et al. 2014) or advective (Churazov et al. 2011; Crocker & Aharonian 2011; Panther et al. 2018b). These interpretations, however, fail to reproduce details in the morphology or violate kinematic constraints. Both scenarios require the transport of positrons over kpc distances. The possibility that a large fraction might annihilate either *in situ* at their sources has attracted little attention. One known but subdominant source is the radioactive isotope ^{26}Al generated in massive star nucleosynthesis. ^{26}Al nuclei create positrons at $\lesssim$MeV energies, hundreds of parsecs away from the stars, implying that the 511-keV emission will not exactly trace ^{26}Al sources. A generalisation of this scenario to other candidate sources is *prima facie* plausible, but has not found supporting evidence, yet.

Here, we attempt to constrain the propagation length of positrons by a spatial analysis of the 511-keV line and the ortho-positronium (ortho-Ps) continuum in the Milky Way bulge from 15 yr of *INTEGRAL*/SPI data. Weidenspointner et al. (2006) reconstructed an image in the energy band 410–500 keV, where ortho-Ps is dominant, and found an asymmetric bulge component. For the first time, we perform a spectrally resolved study of ortho-Ps that extends to lower energies, >200 keV. This leads to an improvement in statistical quality and boosts the discriminant power of existing data because the expected flux of ortho-Ps is about 4–4.5 times larger than that of the 511 keV alone. Including ortho-Ps allows us to compare various spatial tracers of positron annihilation by the use of stellar templates, dark matter (DM) profiles, or disc gas maps, and combinations thereof.

★ E-mail: tho.siegert@gmail.com

2 POSITRON SOURCES IN THE MILKY WAY

Among the most promising sources of positrons are β^+-unstable nucleosynthesis products from thermonuclear supernovae (^{56}Co, ^{44}Ti; e.g. Milne & Leising 1997; Churazov et al. 2015; Diehl et al. 2015; Crocker et al. 2017), massive stars (^{26}Al; e.g. Mahoney et al. 1984; Diehl et al. 2006; Pleintinger et al. 2019), and core-collapse supernovae (^{44}Ti; e.g. Iyudin et al. 1997; Grebenev et al. 2012; Siegert et al. 2015; Grefenstette et al. 2017; Weinberger et al. 2020). Additional, putative sources include compact objects (e.g. Bouchet et al. 1991; Sunyaev et al. 1992; Weidenspointner et al. 2008; Siegert et al. 2016a; Bartels et al. 2018b), such as accreting black holes and magnetized neutron stars, and also DM (e.g. Boehm et al. 2004; Finkbeiner & Weiner 2007; Siegert et al. 2016c). Positrons are also known products in solar flares where they annihilate in the Sun's atmosphere (Murphy et al. 2005), constituting a special case of *in situ* annihilation. Thus, the population of intermittently flaring stars could partly explain the measurements (Bisnovatyi-Kogan & Pozanenko 2017). The stellar population in the Galactic bulge is seen at infrared wavelengths so that *in situ* annihilation may coincide with models describing the nuclear stellar bulge (NB; Launhardt, Zylka & Mezger 2002) and larger boxy bulge (BB; Freudenreich 1998).

The fractional contribution of each of these source populations has not yet been determined, and the identity of a dominant positron source – if such exists – remains subject to debate. A measurement of the characteristic length scale over which positrons propagate through the interstellar medium (ISM) before annihilating may resolve this impasse. This follows from the fact that different source types are characterized by different injection energies, and this strongly determines the maximum distance that positrons can propagate.

The transport of positrons in the ISM is dictated by the Galactic magnetic field, which causes the positrons to scatter or stream along field lines. Their energy losses are determined by collisions with neutral and charged particles (Jean et al. 2009; Martin et al. 2012; Alexis et al. 2014; Panther et al. 2018b). Bremsstrahlung, inverse Compton (IC), and synchrotron emission make subdominant contributions to positron cooling at MeV energies. Positrons in the ISM are expected to propagate until they encounter dense ($> 1\,\mathrm{cm}^{-3}$) neutral gas, when they rapidly start losing their remaining energy and annihilate. Heavier nuclei ($Z > 2$) may also be of importance when considering the annihilation of thermalized positrons (Panther et al. 2018a). If positrons manage to escape their source environments, the final annihilation regions are expected to be traced by CO or HI emission.

MeV γ-ray continuum observations (Strong et al. 2005, 2010) constrain the injection energies of (annihilating) positrons to $\lesssim$3–7 MeV (Beacom & Yüksel 2006; Sizun, Cassé & Schanne 2006). The observed IC morphology provides constraints on where positrons end up thermalising and possibly annihilating 'in flight' (e.g. Aharonian & Atoyan 1981). Instead of slowing down and annihilating, some positrons might also escape the Galaxy in a nuclear outflow associated with the Fermi bubbles (FBs; Su, Slatyer & Finkbeiner 2010; Crocker & Aharonian 2011).

3 EMISSION MODELS

3.1 Template maps

Table 1 gives an overview of positron annihilation emission morphologies tested in this Letter. The template maps may trace either populations associated with emission in the nominated wavelength bands or the emitting population itself. For example, a halo morphology can test for an old population of objects ($\gtrsim$ 1 Gyr), such as Type Ia supernovae, or the stars of the halo themselves.

Table 1. Summary of template maps used in this work. The 'Built' column indicates observed or synthetic templates.

Map	Process/population	Built
BB	Stars (1.25–4.9 μm)	Obs. + syn.
NB	Stars (2.2–240 μm)	Obs. + syn.
XB	Stars (3.4–4.6 μm)	Obs. + syn.
IC	$e^{\pm} + \gamma \rightarrow e^{\pm} + \gamma$	Syn.
CO	CO, $J = 1 \rightarrow 0$ at 115 GHz	Obs.
HI	H, $F = 1 \rightarrow 0$ at 21 cm	Obs.
DM0	DM, $\rho^2_{\mathrm{NFW}}(\gamma = 1.0)$	Syn.
DM2	DM, $\rho^2_{\mathrm{NFW}}(\gamma = 1.2)$	Syn.
FB	Fermi Bubbles (GeV)	Obs. + syn.

If an analytic three dimensional (3D) density distribution is available, we perform line-of-sight (los) integrations to determine the flux per steradian, $F(l, b)$, on a ($50 \times 50\,\mathrm{deg}^2$)-sized grid of pixels with solid angles ($0.5 \times 0.5\,\mathrm{deg}^2$)

$$F(l, b) = \frac{1}{4\pi} \int_{\mathrm{los}} \rho(x(s), y(s), z(s))\mathrm{ds}. \quad (1)$$

Here, $x(s) = x_\odot - s\cos(l)\cos(b)$, $y(s) = y_\odot - \sin(l)\cos(b)$, and $z(s) = z_\odot - s\sin(b)$ is the los vector along Galactic coordinates (l, b).

We tested for bulge populations using a BB template (Freudenreich 1998), an X-shaped Bulge (XB; Ness & Lang 2016), and the NB (Launhardt et al. 2002) population as was used by earlier Fermi-LAT GeV analysis (e.g. Bartels et al. 2018a; Macias et al. 2018). Disc contributions are tested via the Planck CO map (Planck Collaboration X 2016), a los-integrated HI map from 21 cm radio observations (Dickey & Lockman 1990), and energy-dependent IC scattering template maps derived using GALPROP (Strong, Moskalenko & Ptuskin 2007). For IC, we assume one of the best-fitting setups considered in Ackermann et al. (2012) for the analysis of *Fermi*/LAT data, in particular their model $^{\mathrm{S}}\mathrm{L}^{\mathrm{Z}}10^{\mathrm{R}}20^{\mathrm{T}}150^{\mathrm{C}}2$. The halo is modelled either as a Navarro–Frenk–White (Navarro, Frenk & White 1997) DM halo profile with a slope $\gamma = 1.0$ (DM0) or $\gamma = 1.2$ (DM2), or an isotropic emission model with the shape of the FBs (Su et al. 2010). Details on the emission templates are found in the Supplementary Material.

3.2 Three dimensional widening of density profiles

For assessing how similar the initial templates are to the actually measured positron annihilation signal, we perform an additional analysis on the best-fitting images (see Section 5). Widened density profiles $\tilde{\rho}$,

$$\tilde{\rho}(x, y, z; \xi) = \rho(x, y, z) \otimes G(x, y, z; \Sigma), \quad (2)$$

are calculated by convolution ($\otimes$) with a 3D-Gaussian $G(x, y, z; \Sigma)$ with a diagonal covariance matrix $\Sigma = \mathbb{I}\xi^2$ so that each spatial dimension obtains the same smoothing length scale ξ. The resulting 3D-arrays of $\tilde{\rho}$ are then integrated along each los by trilinear interpolation ($(x, y, z) \rightarrow (l, b, s)$). We choose a 3D grid in x and y between -6 and $+6$ kpc, and z between -4 and $+4$ kpc in 50 pc steps, and define a set of ξ values between 0 and 600 pc in 25 pc steps for fits to the data.

4 *INTEGRAL*/SPI DATA ANALYSIS

4.1 Data set

ESA's *INTEGRAL*satellite (Winkler et al. 2003) with its coded-mask γ-ray spectrometer SPI (Vedrenne et al. 2003) has been surveying the sky since 2002. Here, we make use of archival SPI data collected between March 2003 and September 2017, focusing on the Galactic bulge, with a homogeneous exposure of 24.3 Ms in the central $15 \times 15\,\mathrm{deg}^2$. This results in exposures out to $\lesssim 25^\circ$ in l and b, given SPI's large field of view of $16 \times 16\,\mathrm{deg}^2$. After removing outliers in the data set, it comprises 12 587 pointings (targeted observations), with an average observation time of 2313 s, for a total on-time of 29.1 Ms. Up to 2021, four of 19 SPI detectors failed, reducing the sensitivity by ≈ 20 per cent.

We choose six logarithmic energy bands, 189–245, 245–319, 319–414, 414–508, 514–800, and 800–1805 keV, plus a 6-keV broad bin for the 511-keV line, to perform a spatial bin-by-bin analysis. In this way, we are able to capture dominant emission features belonging to positron annihilation, diffuse γ-ray continuum, and point sources.

4.2 General method

SPI data analysis relies on the comparison of sky models and a description of the instrumental background to the raw photon count data. The sky images are convolved through SPI's coded-mask response, which depends on the sources' aspect angles and the photon energy. The background model utilizes knowledge about the instrument, its detectors and shields, and the long-term behaviour in space (Diehl et al. 2018; Siegert et al. 2019a). Models $m_\mathrm{p}(\theta_i)$ are realized as time series of expected detector illuminations, which are fitted to the measured time series d_p via a maximum-likelihood fit using the Poisson likelihood $\mathcal{L}(d_\mathrm{p}|\theta_i)$, determining the fluxes θ_i of model component i. This is done for each energy bin separately. Thus, our model is the superposition of sky and background contributions:

$$m_\mathrm{p} = \sum_t \sum_j R_{jp} \sum_{k=1}^{N_\mathrm{S}} \theta_{k,t} M_{kj} + \sum_{t'} \sum_{k=N_\mathrm{S}+1}^{N_\mathrm{S}+N_\mathrm{B}} \theta_{k,t'} B_{kp}. \quad (3)$$

In equation (3), M_{kj} is the kth of N_S sky models to which the response R_{jp} is applied for each pointing p and pixel j. The $N_\mathrm{B} = 2$ background models B_{kp} are independent of the response. While diffuse Galactic and positron annihilation emission are constant over long periods of time (Purcell et al. 1997), individual sources can change their spectral behaviour on shorter time-scales, which we account for by introducing a point source variability time-scale t. Likewise, the background amplitude can change on a different time-scale t'. We use `SPIMODFIT` v3.2 (Halloin 2009) to perform these fits.

4.3 Model comparisons

For model comparisons, we use the Akaike information criterion (AIC; Akaike 1974). We compute AIC differences ΔAIC to judge the relative importance of model templates compared to a chosen baseline model (Section 4.4). Relative AIC values take into account the differences in the likelihood and the degrees of freedom (ν) so that a model with more parameters can result in a 'worse' fit. Improvements in terms of σ values are estimated by equating the survival probability of a χ^2_ν-distribution to the relative likelihood $\exp(-\Delta\mathrm{AIC}/2)$ (Burnham & Anderson 2004). Because combinations that include DM0+DM2 do not exist in reality we exclude them in the following. In the first bin, 189–245 keV, several point sources contribute to the total flux, but become negligible above 500 keV. As an example, in Fig. 1, we show the gradual improvement in the fit one achieves for a particular concatenation of templates. We choose the optimum combination for positron annihilation, IC+NB+BB (see Section 5.1), as a starting template. The next component is chosen on the basis of which of the remaining provides the largest ΔAIC over the total energy band analysed (189–1805 keV). We proceed in this fashion until the remaining templates are linked.

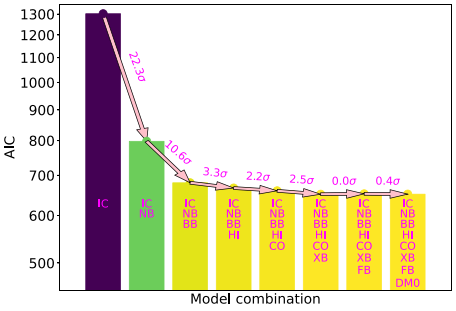

Figure 1. Fit improvements when adding more templates (from the left-hand panel to right-hand panel) for the energy band 189–1805 keV. Relative AIC values convert to σ values.

4.4 Choice of baseline model

The starting point of comparison is not unique and the path towards including more models can be versatile, even improving upon a worse starting point. From previous studies (e.g. Strong et al. 2005; Bouchet et al. 2011; Churazov et al. 2011), it is known to what extent positron annihilation contributes to the soft γ-ray spectrum. Below ≈250 keV, the diffuse Galactic continuum emission as well as (un)resolved point sources dominate the spectrum. Above the 511-keV line, direct annihilation 'in flight' is expected, but has never been detected (e.g. Beacom & Yüksel 2006; Sizun et al. 2006; Churazov et al. 2011), so that these energies can be considered nearly free of positron annihilation. In order to assess annihilation features with respect to different spatial morphologies, a baseline model is established upon which additional components are tested.

First, we evaluated the AIC for each map individually in 'off-annihilation'-bins (excluding 245–514 keV), and then combined them to obtain a solid estimate of which maps are required. We find that the disc-dominated maps IC, HI, and CO, in this sequence, are clearly favoured over any other single map. Using the IC templates, we find $\chi^2 = 589861$ ($\nu = 581570$; $\chi^2/\nu = 1.014$) in these bins combined, suggesting an adequate fit to our data. In a second step, we consecutively add these three maps together to identify possible better baselines. We conclude that 'off-annihilation'-bins are sufficiently described by IC only. For the model comparisons in positron annihilation bins, we thus use IC as a baseline model.

5 RESULTS

5.1 Emission templates and combinations

Between 245 and 514 keV, using the stellar template BB+NB improves the fit above the baseline model by $\Delta\mathrm{AIC}_\pm = 618.2$ (Table 2). This means that the map resembling the projected population of stars in the bulge shows the largest statistical improvement. Including the ortho-Ps continuum provides additional power in discriminating different morphologies, as opposed to only using the 511-keV line. While the template DM0 shows the single best improvement when the 511-keV line is considered in isolation, ortho-Ps provides a

Table 2. Summary of model comparisons.

Baseline model	Add. source	ΔAIC_{511}	ΔAIC_{oPs}	$\Delta AIC_{\pm}$
IC	HI	10.9	4.7	15.6
IC	FB	25.2	9.9	35.1
IC	BB	89.1	192.4	281.5
IC	CO	64.6	239.0	303.6
IC	HI+CO	104.5	278.1	382.6
IC	XB	105.7	289.5	395.2
IC	NB	123.8	383.8	507.6
IC	DM2	134.8	375.8	510.6
IC	DM0	164.3	433.3	597.6
IC	**BB+NB**	**162.0**	**456.2**	**618.2**
IC+BB+NB	CO	− 2.0	− 1.7	− 3.7
IC+BB+NB	DM0	3.6	− 1.1	2.5
IC+BB+NB	CO+HI	− 1.4	16.8	15.4
IC+BB+NB	**HI**	**− 0.3**	**16.3**	**16.0**
IC+BB+NB+HI	DM0	4.8	0.8	5.6
IC+BB+NB+HI+CO	DM0	4.6	1.3	5.9

Note. We show the AIC of additional source templates (second column) with respect to the baseline model for the 511-keV line, the ortho-Ps bins (245–508 keV), as well as positron annihilation as a whole. The second and third sections summarize the search for additional components above the best-fitting BB+NB stellar template.

much sharper discrimination between individual components that favours the stellar templates. The halo template DM2 is significantly worse in all subsequent cases and we only discuss DM0 in the following. Adding more maps to IC+BB+NB results in insignificant improvements. In particular, a contribution from DM morphology is not required in the fit. Putative annihilation region maps (CO/HI) marginally improve the fit in the annihilation band, and not at all in the 511-keV line. Again adding a DM template when gas maps are included (IC+BB+NB+HI+CO+DM0) results in no improvement.

5.2 Similarity between stellar and annihilation morphology

To determine how similar the distribution of stars (BB+NB) is to the actual annihilation emission, we perform a convolution analysis with these two templates and their combination. This increases the number of fitted sky model parameters from three to five. First, the same widening for both templates is used to estimate a common length scale ξ. We find $\xi = 150 \pm 50$ pc (2σ), pointing to a resolvable difference between the initial templates and the annihilation emissions (Fig. 2). To assess which component is more affected, we test the two extremal cases for which only one component is widened, and the other remains unmodified. The NB component is responsible for driving the fit because the smoothing kernel for the BB is only constrained to $\xi_{BB} < 420$ pc (3σ), whereas from the NB we measure a finite smearing of $\xi_{NB} = 150^{+40}_{-70}$ pc (2σ).

6 DISCUSSION

6.1 Supernova kicks

A widened distribution of annihilating positrons could reflect kinematic heating of the initial astrophysical source population due to kicks imparted by asymmetric supernova explosions. Thus, the morphology of the population of compact objects that produce positrons might differ from the parent stellar distribution. We estimate the average kick velocity v_k that would lead to an extended spatial distribution with radius R_k assuming initially virialized objects at

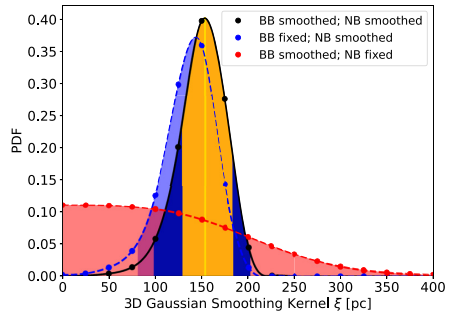

Figure 2. Probability distributions of smoothing widths from the fitted likelihood profile. *Black*: both templates are smoothed by the same ξ. *Blue*: only NB smoothed. *Red*: only BB smoothed. Shown are the 1σ (orange) and 2σ (dark blue) intervals for the first case, the 2σ region for the second (blue), and the 3σ limit (red) for the third.

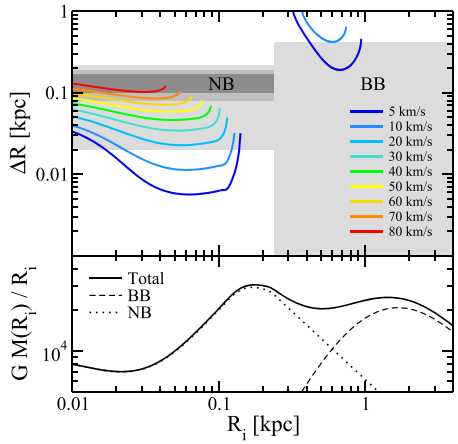

Figure 3. Displacements from an initial radius R_i in the Galactic bulge (NB: top left-hand side, BB: top right-hand side) potential (bottom) for different supernova kick velocities. The grey bands are the regions allowed by our convolution analysis (Dark 1σ, medium 2σ, light 3σ uncertainties).

radius R_i with velocity v_i in the gravitational potential of NB and BB,

$$\frac{1}{2}v_i^2 = \frac{1}{2}G\frac{M(R_i)}{R_i} \overset{\text{kick}}{\Longrightarrow} \frac{1}{2}(v_i^2 + v_k^2) = \frac{1}{2}G\frac{M(R_f)}{R_f}, \quad (4)$$

where $M(R)$ is the cumulative mass profile of the bulge up to radius R, and G is the gravitational constant. We relate the displacement $\Delta R = R_f - R_i$ to the widening length scale, ξ, and illustrate ΔR for different kick velocities in Fig. 3. Within our 3σ limits, the BB only permits small kick velocities $\lesssim 10\,\mathrm{km\,s^{-1}}$. In contrast, the NB requires higher kick velocities, $\gtrsim 20\,\mathrm{km\,s^{-1}}$ also reaching beyond $\approx 100\,\mathrm{km\,s^{-1}}$. Kick velocities of around 5–15 $\mathrm{km\,s^{-1}}$ would match the measurements in both NB and BB (3σ), but with further restrictions on where the sources would be located. In particular, this would mean that sources inhabiting only a fraction of either bulge component could contribute to positrons supplying the observed signals.

Sources may be produced in the NB and BB with small kicks. Globular clusters, for example, retain populations of millisecond pulsars (Song et al. 2021), which must be born with small kicks, $\lesssim$ few tens of $\mathrm{km\,s^{-1}}$, given clusters' typical escape velocities. An alternative millisecond pulsar formation channel that naturally produces low kick velocities ($\lesssim 30\,\mathrm{km\,s^{-1}}$, Tauris et al. 2013), is the accretion induced collapse of one white dwarf. Such a population has recently been suggested in the Galactic bulge (Gautam et al. 2021).

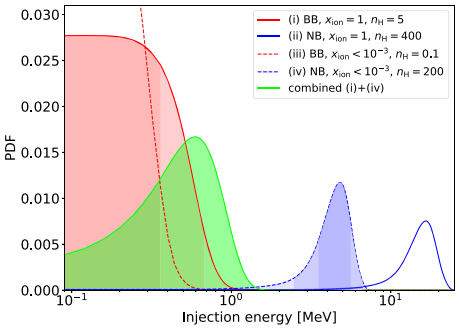

Figure 4. Allowed parameter space for the NB (blue) and BB (red) as a function of injection energy, particle density, and ionisation fraction. Shown are the extremes (ii) and (iii) with the least and largest overlaps (i)+(iv) in green, allowing energies up to ≈1.4 MeV. (Bands: 1, 2, and 3σ bounds).

6.2 Positron propagation

Another possibility to obtain a widened annihilation signal is to have positrons propagating in the ISM before annihilation. To test this, we run Monte Carlo simulations as a function of the ISM density n_H, ionisation fraction x_{ion}, and injection energy E_{inj}. From the canonical ISM phases (Ferrière 2001), cold neutral medium (CNM), warm neutral medium (WNM), warm ionized medium (WIM), and hot ionized medium (HIM), we determine bounds on the positron injection energy in NB and BB independently. In particular, we simulate the interactions of a positron starting at kinetic energy E_{inj} until the distance travelled between two successive interactions drops below 0.1 pc. We include the cross-sections with free and bound electrons, charge exchange, and radiative recombination, energy losses due to ionisation or excitation of hydrogen, plasma losses, bremsstrahlung, synchrotron radiation, and IC scattering. We use a generic magnetic field strength of 50 μG (Ferrière 2009; Crocker et al. 2010). Following the arguments presented by Jean et al. (2009), we assume that various damping processes ensure that there is an insignificant magnetic structure on the 7×10^7 (E_{e^+}/MeV)(50 μG/B) cm gyroradius scale. On the basis of Panther et al. (2018b), we also discount advective transport in a large-scale wind. To account for the uncertain magnetic structure in the bulge, we either (a) follow strictly the results of Jean et al. (2009) with inefficient pitch angle scattering, or (b) apply a complete random walk behaviour after each interaction. This estimates the maximum (a) and minimum (b) distance spread of positrons and, the minimum (a) and maximum (b) injection energy.

We simulate 1000 Monte Carlo packets each for logarithmic grids of n_H in 0.1–10^4 cm^{-3}, x_{ion} in 0–1, and E_{inj} in 0.1–100 MeV for a total of 616 grid points. Each distribution then shows final pseudo-random-walk distances of positrons, scattered around 0, with a width that we relate to the smoothing length scale ξ. In Fig. 4, we show the limiting injection energies from our measured length scales in NB and BB, assuming a complete random walk.

For densities in the NB of 200–400 cm^{-3} (Launhardt et al. 2002), we find injection energies of 0.9–25 MeV reproduce the observed smearing. For the BB, we consider densities of 0.1–5 cm^{-3}. To explain the maximum smoothing scale in the BB of $\lesssim$ 420 pc, positron injection energies of, at most, 1 MeV are possible for a fully ionized medium at rather high density (5 cm^{-3}), which appears unphysical. The resultant annihilation line spectrum in such a medium would contradict the observed spectrum (Guessoum, Jean & Gillard 2005; Siegert et al. 2019b). At lower ionisation fractions, as suggested from spectral measurements (Churazov et al. 2005; Jean et al. 2006), the injection energies would be constrained to values $\lesssim$ 0.9 MeV. While this is consistent with the injection energies found from the NB, the large non-zero propagation lengths in the NB would be in tension with the data from the BB. If the same sources are responsible for positron production in NB and BB, these sources would show injection energies of $\lesssim$1.4 MeV. The results when using the canonical ISM phases for NB and BB are similar in shape but limit the maximum possible injection energy to $\lesssim$0.4 MeV.

7 SUMMARY AND CONCLUSION

In earlier works (e.g. Knoedlseder et al. 2005; Bouchet et al. 2011), it was noted that the 511-keV emission distribution is reminiscent of the old stellar population. Here, we have secured the hypothesized association between annihilating positrons and old stars with a broader, quantitative analysis. Our spatial model fitting demonstrates that stellar templates for the NB and BB best match the positron annihilation γ-ray emission. We show that additional DM templates are not significant, and therefore the DM interpretation of the 511-keV line signal and ortho-Ps continuum is disfavoured.

Still, this match is not perfect and can be systematically improved by introducing a characteristic 150 ± 50 pc (2σ) radial, 3D smoothing of the signal with respect to the underlying stars. While such a widening might indicate a systematic displacement of either positron sources (presumably via natal kicks) or ISM transport of positrons, the former would require differently kicked positron sources in NB and BB. In contrast, the transport scenario can accommodate the different ξ values in NB and BB given the different ISM conditions they present, albeit with some tuning of parameters. Thus, if we hypothesize that the annihilation emission in NB and BB originate from the same source type, the ISM propagation scenario is favoured. This casts some doubt on *in situ* annihilation scenarios.

We determine the distance spread of propagating positrons with initial energy E_{inj} until annihilation when experiencing different ISM conditions. In the NB, we set constraints on the injection energy of $0.9 \lesssim E_{inj}/\mathrm{MeV} \lesssim 25$ (3σ). For the BB, we find $E_{inj} \lesssim 1.0$ MeV (3σ), marginally consistent with the NB. Again, assuming that *the same populations of sources* are responsible for the positrons that annihilate in both the NB and BB, the average injection energy must be at most 1.4 MeV, an energy scale that clearly points to a nucleosynthesis origin of the positrons. This constraint is in line with previous limits on the injection energy from spectral modelling of the annihilation-in-flight continuum (Beacom & Yüksel 2006; Sizun et al. 2006), suggesting $E_{inj} \lesssim$ 3–7 MeV. However, the allowed higher energies in the NB would also include relativistic mechanisms, such as pair production from compact objects. Finally, higher injection energies in the NB and the resulting larger propagation distances would inevitably lead to outflows into the BB.

While *in situ* annihilation at kicked sources is disfavoured when assuming the same positron producers in NB and BB, scenarios with two different source populations should be explored. Dedicated MeV observations and modelling of globular clusters should be considered because at least some compact sources must be born with low kicks. Globular clusters are mostly free of interstellar gas so that cooling of positrons is dominated by IC and synchrotron losses. A detection of a 511-keV signal from globular clusters may require the relaxation of our assumption that all positrons in the Galactic bulge originate from the same source population. Individual globular clusters would be expected to exhibit 511-keV line fluxes of the order of 10^{-6} photons cm^{-2} s^{-1} if a correlation with GeV emission (Bartels et al. 2018b) could be consolidated.

ACKNOWLEDGEMENTS

TS is supported by the German Research Foundation (DFG-Forschungsstipendium SI 2502/3-1). RMC acknowledges support from the Australian Government through the Australian Research Council, award DP190101258 (shared with Prof. Mark Krumholz). OM was supported by the World Premier International Research Center Initiative (WPI Initiative), MEXT, Japan, and by JSPS KAKENHI grant numbers JP17H04836, JP18H04340, JP18H04578, and JP20K14463. FHP is supported by the Australian Research Council (ARC) Centre of Excellence for Gravitational Wave Discovery (OzGrav) under grant number CE170100004. FC acknowledges support from the 'Agence Nationale de la Recherche', grant number ANR-19-CE31-0005-01 (PI: FC). The work of SH and DS is supported by the US Department of Energy Office of Science under award number DE-SC0020262. SH is supported by NSF grants numbers AST-1908960 and PHY-1914409.

DATA AVAILABILITY

The data underlying this Letter will be shared on reasonable request to the corresponding author.

REFERENCES

Ackermann M. et al., 2012, ApJ, 750, 3
Aharonian F. A., Atoyan A. M., 1981, SvA Lett., 7, 395
Akaike H., 1974, IEEE Trans. Autom. Control, 19, 716
Alexis A., Jean P., Martin P., Ferrière K., 2014, A&A, 564, A108
Bartels R., Storm E., Weniger C., Calore F., 2018a, Nat. Astron., 2, 819
Bartels R., Calore F., Storm E., Weniger C., 2018b, MNRAS, 480, 3826
Beacom J. F., Yüksel H., 2006, Phys. Rev. Lett., 97, 071102
Bisnovatyi-Kogan G. S., Pozanenko A. S., 2017, Astrophysics, 60, 223
Boehm C., Hooper D., Silk J., Cassé M., Paul J., 2004, Phys. Rev. Lett., 92, 101301
Bouchet L. et al., 1991, ApJ, 383, L45
Bouchet L., Strong A. W., Porter T. A., Moskalenko I. V., Jourdain E., Roques J.-P., 2011, ApJ, 739, 29
Burnham K. P., Anderson D. R., 2004, Sociological Methods Res., 33, 261
Churazov E., Sunyaev R., Sazonov S., Revnivtsev M., Varshalovich D., 2005, MNRAS, 357, 1377
Churazov E., Sazonov S., Tsygankov S., Sunyaev R., Varshalovich D., 2011, MNRAS, 411, 1727
Churazov E. et al., 2015, ApJ, 812, 62
Crocker R. M., Aharonian F., 2011, Phys. Rev. Lett., 106, 101102
Crocker R. M., Jones D. I., Melia F., Ott J., Protheroe R. J., 2010, Nature, 463, 65
Crocker R. M. et al., 2017, Nat. Astron., 1, 0135
Dickey J. M., Lockman F. J., 1990, ARA&A, 28, 215
Diehl R. et al., 2006, Nature, 439, 45
Diehl R. et al., 2015, A&A, 574, A72
Diehl R. et al., 2018, A&A, 611, A12
Ferrière K. M., 2001, Rev. Mod. Phys., 73, 1031
Ferrière K., 2009, A&A, 505, 1183
Finkbeiner D. P., Weiner N., 2007, Phys. Rev. D, 76, 083519
Freudenreich H. T., 1998, ApJ, 492, 495
Gautam A., Crocker R. M., Ferrario L., Ruiter A. J., Ploeg H., Gordon C., Macias O., 2021, preprint (arXiv:2106.00222)
Grebenev S. A., Lutovinov A. A., Tsygankov S. S., Winkler C., 2012, Nature, 490, 373
Grefenstette B. W. et al., 2017, ApJ, 834, 19
Guessoum N., Jean P., Gillard W., 2005, A&A, 436, 171
Halloin H., 2009, |spimodfit| Explanatory Guide and Users Manual, version 2.9 edn., Physik Max Planck Institut für extraterrestrische Physik, Garching, p. 1
Higdon J. C., Lingenfelter R. E., Rothschild R. E., 2009, ApJ, 698, 350
Iyudin A. F. et al., 1997, in Winkler C., Courvoisier T. J.-L., Durouchoux Ph., eds, ESA SP-382: The Transparent Universe. ESA, Noordwijk, p. 37
Jean P., Knoedlseder J., Gillard W., Guessoum N., Ferrière K., Marcowith A., Lonjou V., Roques J. P., 2006, A&A, 445, 579
Jean P., Gillard W., Marcowith A., Ferrière K., 2009, A&A, 508, 1099
Johnson W. N. I., Haymes R. C., 1973, ApJ, 184, 103
Knoedlseder J. et al., 2005, A&A, 441, 513
Launhardt R., Zylka R., Mezger P. G., 2002, A&A, 384, 112
Macias O., Gordon C., Crocker R. M., Coleman B., Paterson D., Horiuchi S., Pohl M., 2018, Nat. Astron., 2, 387
Mahoney W. A., Ling J. C., Wheaton W. A., Jacobson A. S., 1984, ApJ, 286, 578
Martin P., Strong A. W., Jean P., Alexis A., Diehl R., 2012, A&A, 543, A3
Milne P. A., Leising M. D., 1997, in Dermer C. D., Strickman M. S., Kurfess J. D., eds, AIP Conf. Ser. Vol. 410, Proceedings of the Fourth Compton Symposium. Am. Inst. Phys., New York, p. 1017
Murphy R. J., Share G. H., Skibo J. G., Kozlovsky B., 2005, ApJS, 161, 495
Navarro J. F., Frenk C. S., White S. D. M., 1997, ApJ, 490, 493
Ness M., Lang D., 2016, AJ, 152, 14
Panther F. H., Seitenzahl I. R., Crocker R. M., Machacek J. R., Murtagh D. J., Siegert T., Diehl R., 2018a, Phy. Rev. D, 98, 023015
Panther F. H., Crocker R. M., Birnboim Y., Seitenzahl I. R., Ruiter A. J., 2018b, MNRAS, 474, L17
Planck Collaboration X, 2016, A&A, 594, A10
Pleintinger M. M. M., Siegert T., Diehl R., Fujimoto Y., Greiner J., Krause M. G. H., Krumholz M. R., 2019, A&A, 632, A73
Prantzos N., 2006, A&A, 449, 869
Prantzos N. et al., 2011, Rev. Mod. Phys., 83, 1001
Purcell W. R. et al., 1997, ApJ, 491, 725
Siegert T., Diehl R., Krause M. G. H., Greiner J., 2015, A&A, 579, A124
Siegert T. et al., 2016a, Nature, 531, 341
Siegert T., Diehl R., Khachatryan G., Krause M. G. H., Guglielmetti F., Greiner J., Strong A. W., Zhang X., 2016b, A&A, 586, A84
Siegert T., Diehl R., Vincent A. C., Guglielmetti F., Krause M. G. H., Boehm C., 2016c, A&A, 595, A25
Siegert T., Diehl R., Weinberger C., Pleintinger M. M. M., Greiner J., Zhang X., 2019a, A&A, 626, A73
Siegert T., Crocker R. M., Diehl R., Krause M. G. H., Panther F. H., Pleintinger M. M. M., Weinberger C., 2019b, A&A, 627, A126
Sizun P., Cassé M., Schanne S., 2006, Phys. Rev. D, 74, 063514
Song D., Macias O., Horiuchi S., Crocker R. M., Nataf D. M., 2021, MNRAS, 507, 5161
Strong A. W., Diehl R., Halloin H., Schönfelder V., Bouchet L., Mandrou P., Lebrun F., Terrier R., 2005, A&A, 444, 495
Strong A. W., Moskalenko I. V., Ptuskin V. S., 2007, Annu. Rev. Nucl. Part. Sci., 57, 285
Strong A. W., Porter T. A., Digel S. W., Jóhannesson G., Martin P., Moskalenko I. V., Murphy E. J., Orlando E., 2010, ApJ, 722, L58
Su M., Slatyer T. R., Finkbeiner D. P., 2010, ApJ, 724, 1044
Sunyaev R. et al., 1992, ApJ, 389, L75
Tauris T. M., Sanyal D., Yoon S. C., Langer N., 2013, A&A, 558, A39
Vedrenne G. et al., 2003, A&A, 411, L63
Weidenspointner G. et al., 2006, A&A, 450, 1013
Weidenspointner G. et al., 2008, Nature, 451, 159
Weinberger C., Diehl R., Pleintinger M. M. M., Siegert T., Greiner J., 2020, A&A, 638, A83
Winkler C. et al., 2003, A&A, 411, L1

SUPPORTING INFORMATION

Supplementary data are available at *MNRASL* online.

Please note: Oxford University Press is not responsible for the content or functionality of any supporting materials supplied by the authors. Any queries (other than missing material) should be directed to the corresponding author for the Letter.

This paper has been typeset from a TEX/LATEX file prepared by the author.